

Journal of Mechanics of Materials and Structures

**DAMAGE DEVELOPMENT IN AN ARMOR ALUMINA IMPACTED WITH
DUCTILE METAL SPHERES**

Brett G. Compton, Eleanor A. Gamble, Vikram S. Deshpande and Frank W. Zok

Volume 7, No. 6

June 2012

DAMAGE DEVELOPMENT IN AN ARMOR ALUMINA IMPACTED WITH DUCTILE METAL SPHERES

BRETT G. COMPTON, ELEANOR A. GAMBLE, VIKRAM S. DESHPANDE AND FRANK W. ZOK

The present article describes a coupled experimental/computational study of damage development in confined ceramic tiles impacted by spherical metal projectiles. The principal objective is to calibrate the material parameters in the Deshpande–Evans constitutive model for an armor alumina and assess its utility in predicting trends in damage development with impact velocity. The nature of the damage at the impact site is probed through optical and scanning electron microscopy of cross-sections through the impact site as well as surface profile measurements. Once calibrated, the model is used in finite element simulations and shown to predict reasonably accurately the variation in the size of the comminuted zone beneath the impact site with incident projectile velocity. The numerical simulations also provide new insights into the spatial and temporal evolution of subsurface damage and deformation processes as well as the role of metal face sheets in these processes.

1. Introduction

The ballistic performance of ceramics cannot be readily predicted solely on the basis of material composition and microstructure nor on the basis of common physical and mechanical properties. Consequently, the pathway to developing better materials for armor systems remains ill-defined. The goal of the present study is to advance the understanding of the connections between ballistic resistance and intrinsic material properties of ceramics. The study consists of a coupled experimental/computational study of damage development in confined ceramic tiles impacted by spherical metal projectiles. The computational portion utilizes a mechanistic model of ceramic deformation in which the calibrating parameters relate directly to normative material properties. Through numerical simulations of representative impact scenarios, the model has the potential to identify the key microstructural characteristics that govern ballistic performance and hence guide the directions of future material development activities. It could also prove to be an effective tool in the design of armor systems.

Although the relationships between failure mechanisms and material properties during ballistic impact have been studied extensively [Ashby and Sammis 1990; Compton et al. 2011; Longy and Cagnoux 1989; Rhee et al. 2001; Shih et al. 2000], no consensus exists on exactly how hardness, toughness and strength affect ballistic performance. In regard to penetration resistance, hardness, H , is arguably the most important material property; a hard material is more effective than a soft one at deforming and eroding an impacting projectile. Fracture toughness, K_C , is a second. A material with low toughness has greater propensity for fragmentation and comminution at an impact site, rendering the material ineffective at further impeding projectile penetration. But the tradeoffs between these two properties — H and K_C — are poorly understood. For instance, altering material composition or microstructure to increase

Keywords: impact, ceramic, damage, microcracking.

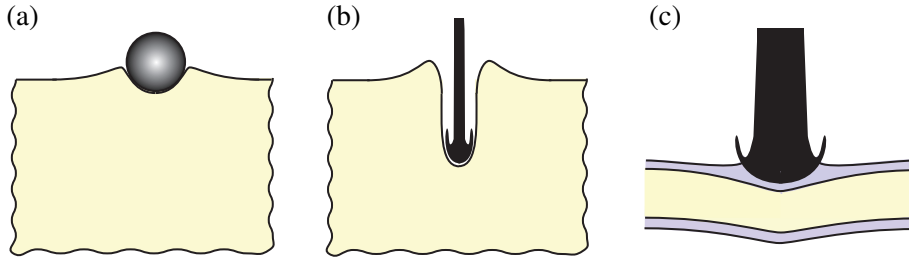


Figure 1. Model impact scenarios used to probe material responses and assess material models: (a) penetration initiation; (b) deep penetration; (c) trilayer penetration.

hardness usually results in a lower toughness, and vice versa [Chantikul et al. 1990]. Predicting with confidence whether the combined changes improve or diminish ballistic performance is presently not possible. Furthermore, it is unlikely that property changes have the same effect under all impact scenarios.

The Young's modulus, E , and the mass density, ρ , can also play important roles. For instance, a material with a high acoustic impedance, $\sqrt{E\rho}$, generates a higher stress on an impacting projectile and is thus more effective at impeding penetration. Naturally the benefits of a material with higher density come at the expense of increased system weight (assuming that volume is held fixed).

With the goal of establishing connections between ballistic performance and material properties, Deshpande et al. [2011] devised a mechanistic constitutive model for deformation and damage of ceramics. The model has been coded as a user-material subroutine for use in the finite element code ABAQUS. Three modes of deformation are included: dislocation plasticity, distributed microcracking, and granular flow of fully comminuted material. Additional details of the model are presented below.

The study is part of a broader effort to probe, both experimentally and computationally, the features associated with various impact scenarios and the effects of material properties. Three such scenarios are illustrated in Figure 1. The one in (a)—penetration initiation—is the focus of the present paper. The second (b) deals with deep penetration by long-rod projectiles and the third (c) involves penetration through ceramic/metal multilayers. Analyses and simulations of the latter scenarios will be presented elsewhere.

The predictive capabilities of this model in the quasi-static deformation regime were demonstrated in [Gamble et al. 2011]. The principal objective of the present study is to assess the capabilities of the DE model in the *dynamic deformation regime* for predicting *damage initiation and growth* in a ceramic in the vicinity of an impact. This is accomplished through comparisons between numerical simulations and experimental observations on impact damage in an armor ceramic. A secondary objective is to relate the damage development sequence during impact to the temporal evolution of contact pressure and force at the impact site.

2. Materials and experimental methods

Experiments were conducted on a fine-grained armor-grade ceramic (Corbit 98, produced by Industri Bitossi and characterized in [Gamble et al. 2011; Denzel 2010]). The material consists of 98% alumina and minor amounts of a glassy phase at the grain boundaries. It was obtained and tested in the form of 50 mm \times 50 mm \times 12 mm tiles.

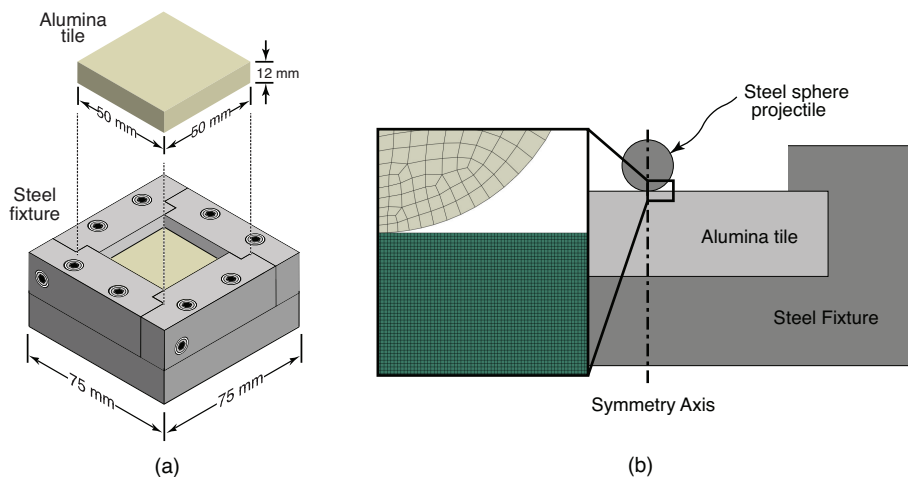


Figure 2. (a) Schematic of alumina target and steel fixture used for impact tests. (b) The corresponding finite element geometry and mesh.

Impact tests were conducted in one of two light-gas guns using either helium or nitrogen as the propellant. Each tile was inserted and clamped within a steel fixture, illustrated in Figure 2. To ensure intimate contact between the tile face and the fixture, 0.1 mm thick steel shims were placed between all lateral faces. Additionally, to protect the back plate of the fixture, a sacrificial 1 mm thick annealed 4130 steel sheet was placed between the back face of the tile and the fixture. The fixture was bolted together and tightened to roughly 10 MPa lateral compression. In some instances, a sheet of 304 stainless steel (either 0.5 or 1 mm thick) was placed on the front face of the ceramic target, to assess the effects of such sheets on the damage process. The target assembly was then mounted in the gas gun against a thick steel backing. The target was impacted with a 304 stainless steel sphere, either 7.6 or 7.15 mm in diameter (depending on the sabot design for the two gas guns). Spheres were obtained from Salem Specialty Ball Company and McMaster-Carr. Tests were performed at velocities in the range 250–800 m/s. Velocities were measured by laser gates.

Following impact, the tile was removed from the test fixture, coated with a dye-penetrant (to enhance viewing of cracks) and imaged using macro-photography. Surface profiles of the tile at and around the impact site were measured using a Wyko NT1100 Optical Profiling SystemTM. To image subsurface damage, the tiles were first cast in epoxy (to prevent material loss during subsequent operations) and sectioned through the point of impact with a diamond wafering blade. As-cut surfaces were sufficient to identify the presence and approximate size of the comminuted regions as well as the cone and radial cracks via macro-photography. In some instances, the sectioned surfaces were polished to 0.5 μm finish and subsequently examined with optical and scanning electron microscopy.

3. Experimental observations and measurements

The key experimental results are illustrated in Figures 3–5. They reveal the following trends.

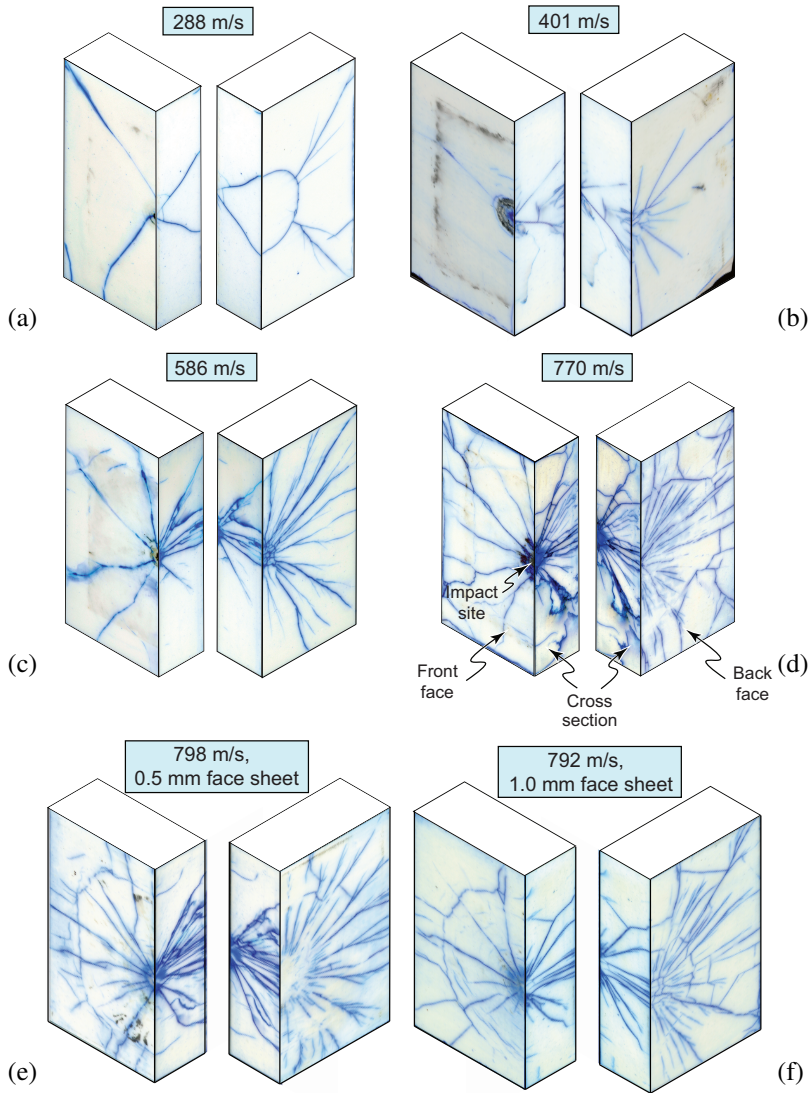


Figure 3. Crack patterns and damage in impacted alumina tiles.

At low impact velocities, defined by $V_0 < 350$ m/s, a single dominant cone crack is observed emanating from the impact site with no evidence of a residual crater (Figure 3a). At slightly higher velocities, typically 350–400 m/s, the cone crack is accompanied by a small number (5–10) of radial cracks, principally on the back face, but also present to a lesser extent on the impact face. The first indications of a permanent crater appear, manifested as slight surface depressions ($\approx 1\text{--}5\ \mu\text{m}$). Within the resolution of the imaging techniques employed in this study, there does not appear to be evidence of microcracking at the impact site in this velocity range.

More dramatic changes are observed at velocities ≥ 500 m/s. In addition to increased densities of cone cracks and radial cracks, the crater becomes more pronounced and a well-defined comminuted zone directly beneath the impact site emerges. The latter zone is manifested macroscopically as a distinct

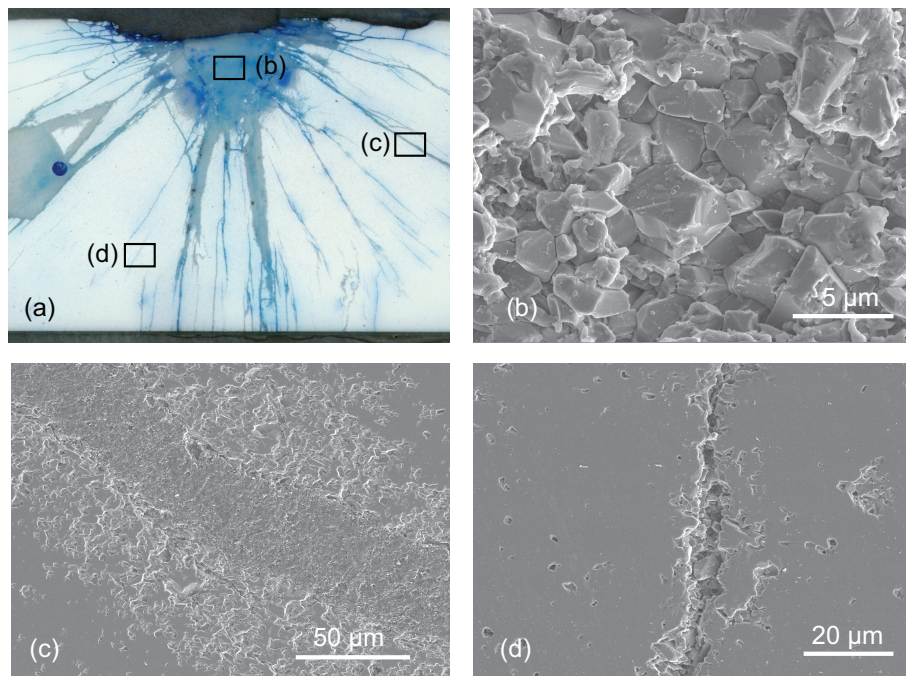


Figure 4. Cross-section through specimen impacted at 778 m/s. (a) Optical overview of the damage zone. (b) SEM image of the comminuted region. (c) A dominant cone crack. The central 50 μm wide band is epoxy that had filled the crack during sample preparation. Flanking this are 50 μm wide strips of microcracked material. (d) A relatively sharp crack with no adjacent comminution.

concentrated patch of dye penetrant. The nature of the damaged region was elucidated from examinations of polished cross-sections in a scanning electron microscope (SEM). Representative images are shown in Figure 4. These confirm that the region of high penetrant concentration is indeed due to comminution. That is, despite the polishing, the images reveal (unpolished) granules with dimensions comparable to the grain diameter (3 μm). Virtually all grains are separated from their neighbors in this region. One consequence is that, upon polishing, the near surface grains are pulled out, exposing the underlying comminuted material.

Similar features are observed in the regions flanking some of the “wider” cone cracks. In the example shown in Figure 4c, the central region (about 50 μm wide) has been filled with epoxy during mounting. On either side of the crack, the material has been polished to some extent, although damage, in the form of grain pullout, is clearly evident. The present interpretation is that these regions represent *damage bands* that form in conjunction with the cone cracks. Precise definition of their boundaries and the extent of comminution within these bands is not possible using the present sectioning and polishing technique, largely because of the extreme friability of the damaged material coupled with incomplete infiltration of the supporting epoxy (especially if contiguous paths to the free surfaces are lacking). In other cases, such as that shown in Figure 4d, single dominant cracks are obtained without damage in adjacent material. These are reminiscent of cone cracks found under quasi-static loading conditions.

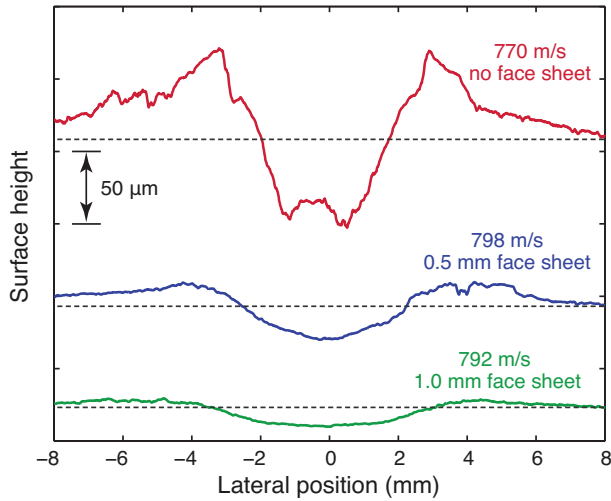


Figure 5. Surface profiles after impact. Dashed lines represent approximate locations of initial surfaces.

In the highest velocity range probed (750–800 m/s), the presence of a thin (0.5 or 1.0 mm) sheet on the impact face has two important effects. First, the size of the comminuted zone is significantly reduced. Indeed, for a sheet thickness of 1.0 mm, comminution is virtually non-existent (Figure 3f). However, there does not appear to be a significant change in the pattern of macroscopic radial and cone cracks (compare Figures 3d–3f). The second is a reduction in the depth of the crater produced upon impact. For instance, absent an outer sheet, the crater depth is $100\ \mu\text{m}$; for a 1 mm sheet, the depth is $<20\ \mu\text{m}$ (Figure 5). The benefits associated with the metal face sheet are addressed by finite element calculations presented in a subsequent section.

4. Numerical simulations of damage growth

A numerical analysis of damage evolution within the alumina tiles follows. The principal goal is to assess the capabilities and limitations of the Deshpande–Evans constitutive model for ceramics.

4.1. Finite element geometry. Axisymmetric finite element calculations of impact were performed using ABAQUS/Explicit V6.9-EF. The projectile was represented by a graded, unstructured quad mesh. The element sizes ranged from $180\ \mu\text{m}$ (R/20) at the point of initial contact to roughly $700\ \mu\text{m}$ (R/5) on the opposite side. This mesh was capable of accommodating the distortions in the projectile during impact without resorting to element deletion. The ceramic tile was meshed using structured quad elements, $60\ \mu\text{m}$ on a side, over the entire area. Its diameter was selected to coincide with the width of the actual tiles (50 mm). The steel fixture was meshed using unstructured quad elements, nominally $350\ \mu\text{m}$ in size (Figure 2b), with appropriate inner diameter (to match the test specimen geometry) and clamp dimensions (to match those in the experiments).

4.2. Constitutive laws for projectile and face sheet. The projectile and the face sheet were modeled using the von Mises yield criterion and the Johnson–Cook constitutive law for both strain and strain-rate

	projectile (304 steel)	face sheet (annealed 304 steel)		projectile (304 steel)	face sheet (annealed 304 steel)
<i>A</i>	1100 MPa	260 MPa	T_m	1800 K	1800 K
<i>B</i>	610 MPa	1350 MPa	T_0	300 K	300 K
<i>n</i>	0.4	0.62	c_p	450 J/kg K	450 J/kg K
<i>m</i>	0.82	1.0	Inelastic heat fraction	0.9	0.9
<i>C</i>	0.013	0.02			
$\dot{\epsilon}_0$	1.0	1.0			

Table 1. Johnson–Cook parameters for steels used in the finite element analyses.

hardening as well as thermal softening. The pertinent material parameter values are listed in Table 1. These parameters were obtained in part from a parallel investigation of the flow properties of 304 stainless steel sheet [unpublished data] as well as data reported in the literature [Stout and Follansbee 1986]. Additionally, both the projectile and the face sheets were assumed to be adiabatic during the impact, consistent with observations of heat tinting and some melting on recovered projectile fragments and face sheets.

To enable the computations to run to completion (up to and beyond projectile rebound), the large distortions in the face sheet (when used) were handled by assigning a large plastic failure strain ($\epsilon_{pl} = 4$) to this material and subsequently deleting the failed elements. Although the failure strain is selected somewhat arbitrarily, it has virtually no effect on the results presented here, since face sheet failure (regardless of whether the failure strain is selected to be 1 or 4) does not initiate until long after the damage within the ceramic has reached its terminal state.

4.3. Constitutive law for ceramic.

Model description. The alumina in the simulations is represented by the extended Deshpande–Evans (DE) constitutive model. Explicit formulations are presented in [Deshpande et al. 2011]. The model accounts for three inelastic deformation mechanisms.

Lattice plasticity is described by standard power law relations between equivalent stress, plastic strain and strain rate. The key material properties are the initial yield stress, σ_Y , the strain hardening exponent, M , the reference strain rate, $\dot{\epsilon}_0$, the strain rate sensitivity exponent, n , and the transition strain rate, $\dot{\epsilon}_t$, at which dislocation velocity becomes limited by phonon drag.

Distributed microcracking is described by a generalization of Ashby and Hallam’s model for wing crack extension under compressive stress states [Ashby and Hallam 1986]. Two non-dimensional parameters characterize the initial damage state: the initial flaw size, $g_1 \equiv a_0/d$, and the flaw spacing, $g_2 \equiv s/d = (f^{1/3}d)^{-1}$ where d is the average grain size, s is the flaw spacing and f is the number of flaws per unit volume. Three behavioral regimes are obtained, delineated by the stress triaxiality, $\lambda \equiv \sigma_m/\sigma_e$ (σ_m being the mean stress). In Regime I, pre-existing cracks are closed and the shear stress is insufficient to overcome the frictional resistance of the contacting crack surfaces. Consequently, the mode I crack tip stress intensity is zero and crack growth cannot occur. This behavior is obtained when the stress triaxiality is less than a critical value, λ_C : dictated largely by the friction coefficient, μ , of the crack surfaces and the current level of microcrack damage. For friction coefficients typical of engineering ceramics, $\lambda_C \approx -0.5$ to -1 . At higher triaxialities, in Regime II, the crack surfaces remain in contact

but are able to slide past one another. Sliding leads to a finite stress intensity which drives the formation of wing cracks at the tips of existing flaws. The cracks extend, initially stably, and eventually link to produce a fully comminuted ceramic. Following [Aeberli and Rawlings 1983], the crack growth rate is taken to scale with $(K_I/K_{IC})^m$ where $m \approx 30$. The crack growth rate is further restricted from exceeding the shear wave speed of the uncracked material. In Regime III, at yet higher triaxialities, the cracks are open and thus behave as Griffith-type defects.

The competition between microcracking and plasticity — as manifested in the relative positions of the yield surface and the damage initiation surface in stress space — is set by the ductility parameter, Δ , defined by (see [Horii and Nemat-Nasser 1986])

$$\Delta \equiv \frac{K_{IC}}{\sigma_Y \sqrt{\pi a_0}} = \frac{K_{IC}}{\sigma_Y \sqrt{\pi g_1 d}}. \quad (1)$$

One implication is that, for constant yield strength, the same damage behavior would be expected for combinations of fracture toughness and flaw size for which $K_{IC}/\sqrt{a_0}$ is constant.

Following crack coalescence, *granular flow* can occur by rotation and sliding of the resulting comminuted particles. Granular flow is taken to obey the linear Drucker–Prager yield criterion, characterized by a critical strength σ_e^{cr} at $\sigma_m = 0$ and a friction angle ω , and with a linear plastic potential, characterized by a dilation angle, ψ . Associated flow is obtained by setting $\psi = \omega$, whereupon the plastic strain exhibits significant dilation. At the other extreme, where $\psi = 0$, the granular plastic strain is purely deviatoric.

Calibration procedure. Calibration of the DE model was performed in the following way. Where possible, input parameters were taken or inferred from direct measurement. For example, density was measured using the Archimedes method, the elastic modulus was calculated from ultrasonic wave speed measurements [Denzel 2010], and plasticity parameters were taken from previously reported quasi-static indentation tests and associated numerical analyses [Gamble et al. 2011]. Tensile (fracture) properties were calibrated to the measured biaxial flexure strength, $\sigma_f = 355 \pm 12$ MPa (J. Shaw and M. Rossol, private communication). Confirmation of the selected plastic properties ($M = 0.1$, $n = 34$, $\sigma_Y = 5.75$ GPa) was accomplished by comparing numerical simulations to the results of a series of 1D plate impact experiments reported in [Denzel 2010]. Comparisons between computed and measured particle velocities U_P for plate impact are shown in Figure 6. Also shown are the results of parametric studies of the effect of the hardening and rate sensitivity exponents. Using the yield strength and hardening values inferred from quasi-static indentation and a linear pressure-density relationship, the experimental particle velocity traces and Hugoniot elastic limit (HEL) are reproduced remarkably well. Further details on the shock response are presented [Denzel 2010].

For parameters not amenable to direct measurement or inference, a narrow range of realistic values was identified and parameter sensitivity studies were conducted at one impact velocity (750 m/s, no face sheet). For instance, the mode I long-crack fracture toughness of the alumina of present interest is $2.9 \text{ MPa}\sqrt{\text{m}}$. However, since the microcracks that form beneath the indent are inherently short and generally experience combined mode I/II loading, the pertinent toughness may differ somewhat from this value. To cover the range of realistic possibilities, the fracture toughness values investigated in the present computations span the range 2.5 to $3.5 \text{ MPa}\sqrt{\text{m}}$. A realistic range for the initial flaw size a_0 for microcracking is identifiable as well. Assuming the existence of flaws on grain boundary facets, the flaw size is $g_1 \equiv a_0/d \approx 1/4$. Alternatively, if flaws are initiated by slip within the grains, the flaw size is

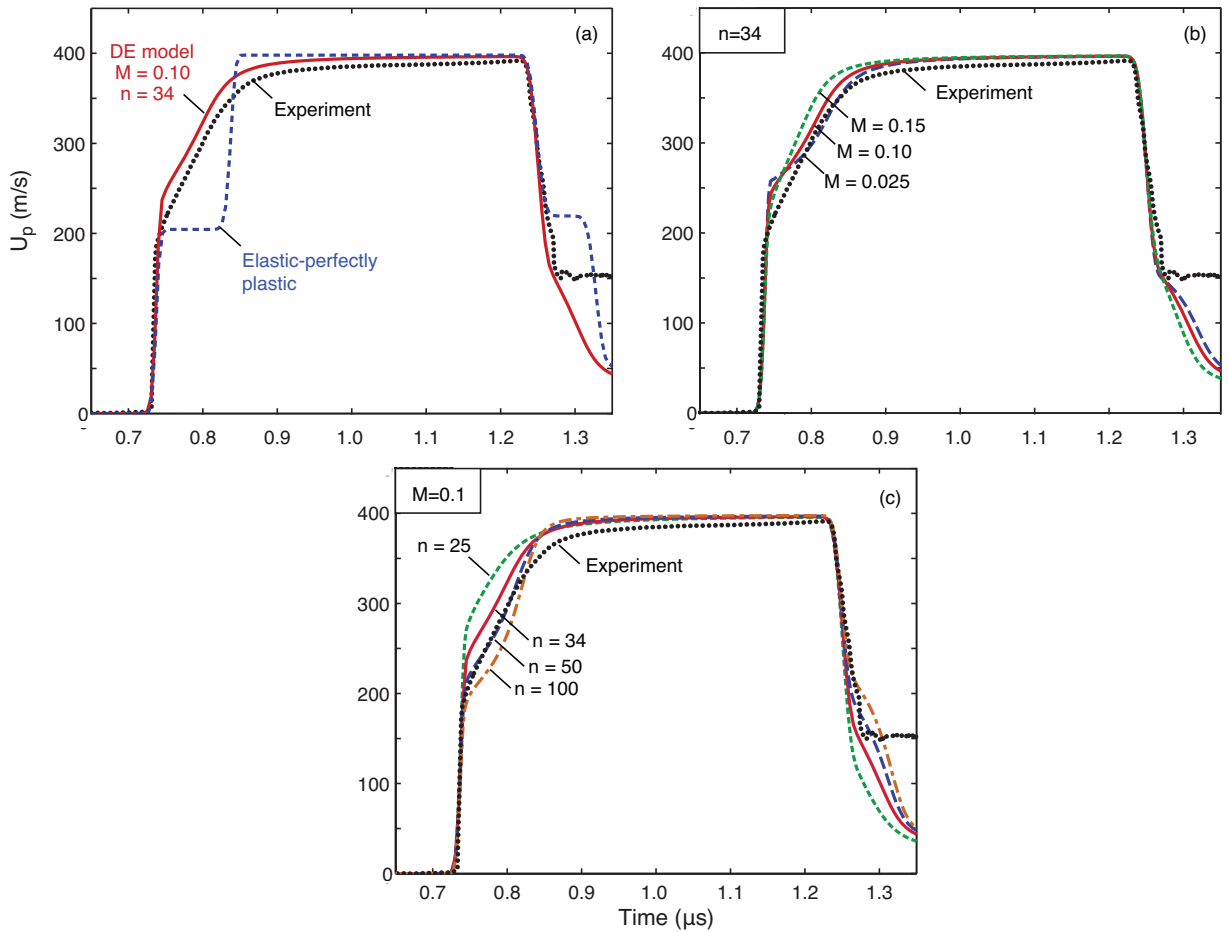


Figure 6. Experimental measurements of the one-dimensional shock loading response of alumina and effects of strain hardening and strain rate hardening in the predicted response from the DE model.

$g_1 \approx \frac{1}{2}$. Thus the range of interest for the computations is expected to be bounded approximately by $\frac{1}{4} \leq g_1 \leq \frac{1}{2}$. The flaw spacing parameter, g_2 , and dilation angle, ψ , are more difficult to estimate *a priori*. But, as demonstrated below, the computed results are insensitive to their values over a rather broad range ($3 \leq g_2 \leq 12$, $0 \leq \psi \leq 35^\circ$).

The results of the parametric studies used for model calibration (for an impact velocity of 750 m/s, without a face sheet) are shown in Figures 7 and 8. Comparisons with observed damage patterns through transverse cross-sections show that a reasonably good match is achieved for a fracture toughness $K_{IC} = 3 \text{ MPa}\sqrt{\text{m}}$ and a flaw spacing $g_1 = \frac{1}{2}$: both falling within their respective expected ranges. They also confirm the insensitivity of the damage patterns to flaw spacing, g_2 , and dilation angle, ψ , over the range $0 \leq \psi \leq 35^\circ$. Similar insensitivity was found in an earlier study on quasi-static indentation [Gamble et al. 2011]. All subsequent numerical simulations utilize $g_2 = 6$ and $\psi = 0^\circ$. These and other material parameter values employed in the subsequent simulations are summarized in Table 2.

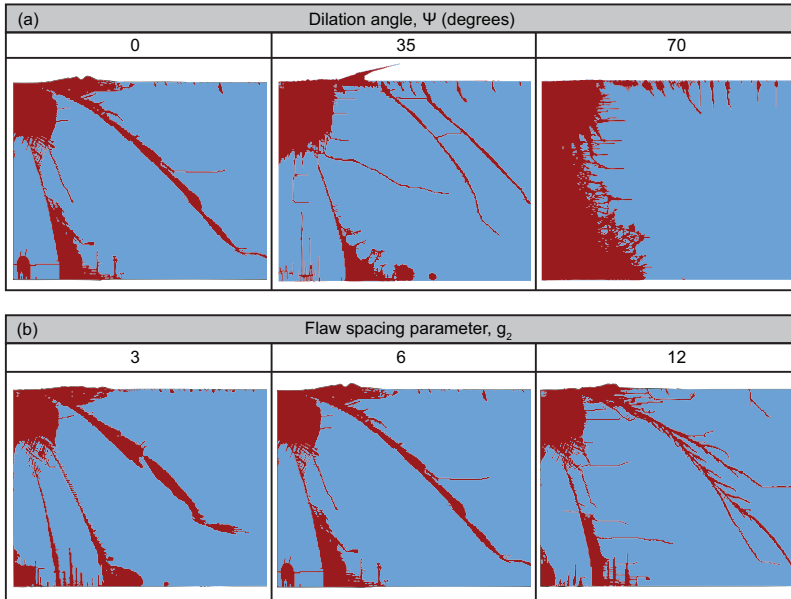


Figure 7. Effects of (a) dilation angle and (b) flaw spacing on damage zone for impact at 750 m/s.

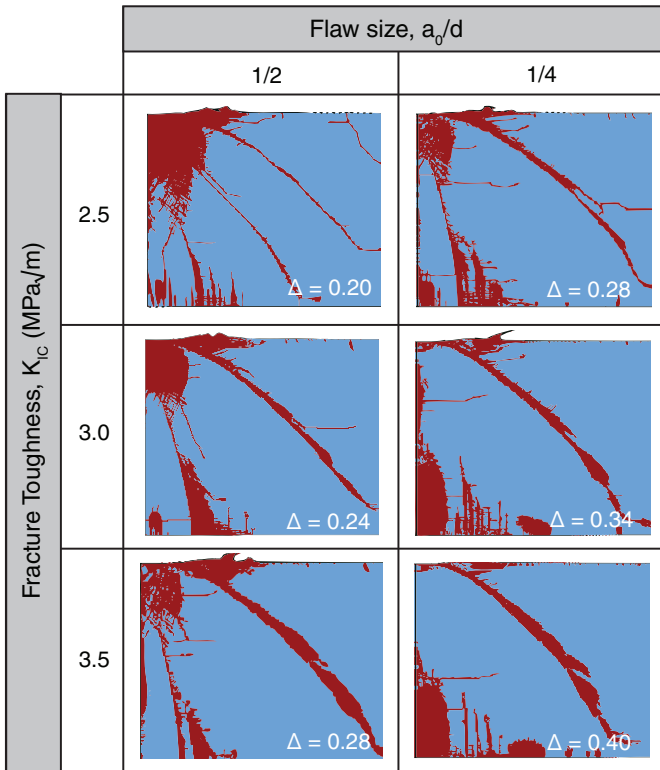


Figure 8. Effect of fracture toughness and flaw size as well as ductility parameter, Δ , on the predicted damage zone size in alumina impacted at 750 m/s.

Parameter	selected value	range considered
Density, ρ (kg/m ³)	3864	
Poisson's ratio, ν	0.239	
Young's modulus, E (GPa)	366	
Grain diameter, d (μm)	3.0	
Yield stress, σ_Y (GPa)	5.75	
Fracture toughness, K_{IC} (MPa $\sqrt{\text{m}}$)	3.0	2.5–3.5
Strain hardening exponent, M	0.1	0.025–0.15
Crack growth rate sensitivity exponent, m	30	
Strain rate dependence exponent, n	34	25–500
Reference crack growth rate, \dot{l}_0 (m/s)	0.01	
Reference strain, ϵ_0	0.002	
Reference plastic strain rate, $\dot{\epsilon}_0$ (1/s)	0.001	
Normalized flaw size, g_1	0.5	0.25, 0.5
Normalized flaw spacing, g_2	6	3–12
Crack geometry factor, γ	6	4–8
Crack coefficient of friction, μ	0.75	
Transition shear strain rate, $\dot{\epsilon}_t$ (1/s)	10^6	
Soil friction angle, ω	70°	
Soil uniaxial compressive strength, σ_C (MPa)	1	
Soil transition exponent, χ_d	5	
Soil transition strain rate, $\dot{\epsilon}_{\text{cut-off}}$ (1/s)	$2 \cdot 10^6$	
Dilation angle, ψ	0°	0° – 70°

Table 2. Summary of alumina property data used in the extended DE model.

4.4. Numerical results. Using the material parameter set ascertained from the preceding calibrations, additional simulations were performed over a velocity range corresponding to that in the experiments. Comparisons of subsurface damage zones for direct impact are presented in Figure 9. Effects of the metal face sheet are shown in Figure 10. The numerical predictions match experimental observations remarkably well over the entire range of impact velocities and loading conditions investigated. Notably, they capture the general features of the size of the comminuted region directly beneath the impact, the formation of conical damage bands emanating from the impact site, and the damage that emanates from the back face as a result of stress wave reflections and/or bending at the tile/fixture interface. They also correctly capture the reduction in the size of the comminuted zone with the addition of metal sheets on the impact face. Indeed, for a 1 mm thick face sheet, the simulations correctly predict that no comminution occurs directly beneath the impact site.

The results from the numerical simulations have also been analyzed to enable improved understanding of contact pressure and force history as well as the damage evolution process. Representative results, for $V_0 = 750$ m/s, are plotted in Figures 11–13. Absent a face sheet, the maximum contact pressure occurs

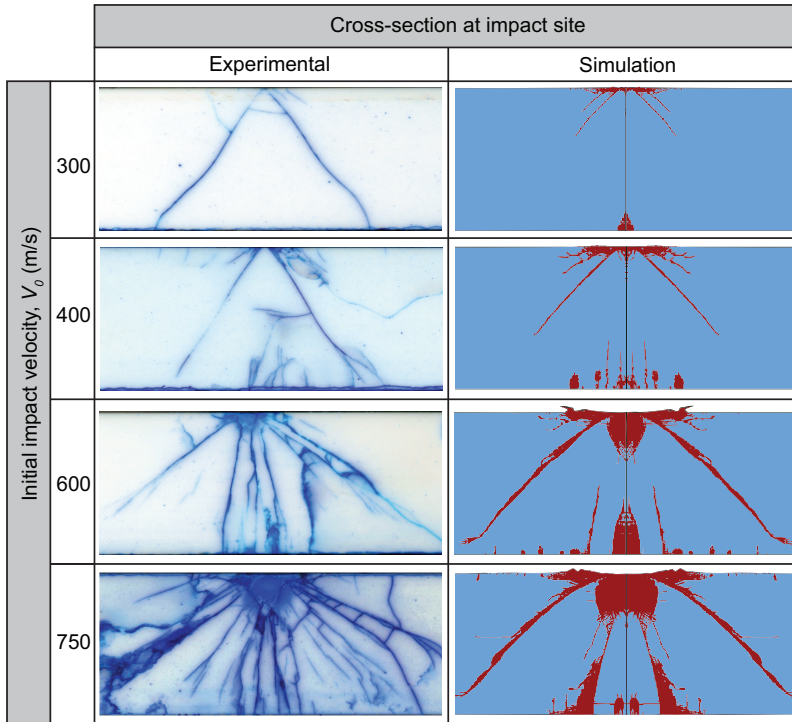


Figure 9. Computed and observed damage patterns. Computed results taken at 17 ms from first contact (immediately after projectile rebound). Experimental impact velocities are within ± 20 m/s of the indicated velocity.

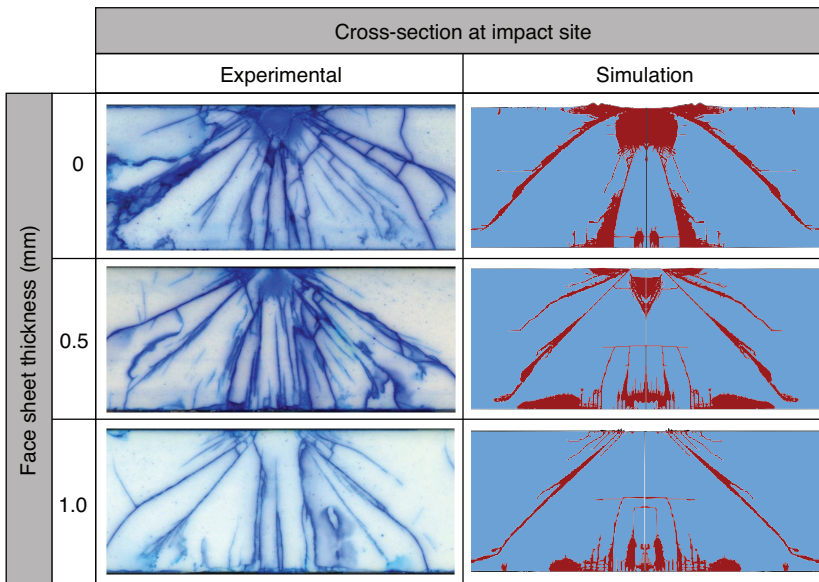


Figure 10. Effects of face sheet thickness on computed and observed damage patterns for impact velocity of 750 ± 20 m/s. Computed results taken at 17μ s after first contact.

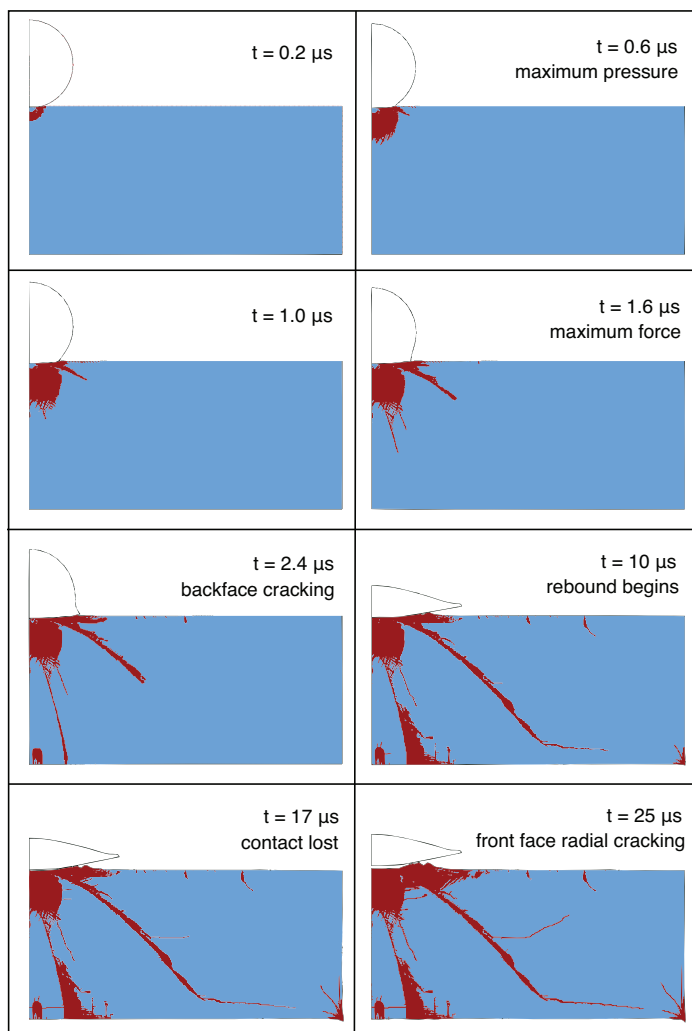


Figure 11. Progression of damage with time after impact for impact velocity of 750 m/s.

very shortly after impact ($< 1 \mu\text{s}$). The pressure then drops quickly, reaching half its peak value within $2 \mu\text{s}$. The corresponding sequence of damage events falls into three time domains.

- (1) At short times (comparable to that at peak pressure), the damage zone grows in a roughly hemispherical pattern at the impact site. As the contact pressure falls and the magnitude of the stress waves in the ceramic is diminished, the conditions for further microcracking are no longer met and the damage ceases. For the example in [Figure 11](#), the critical time for the latter event is about $1.6 \mu\text{s}$ after impact.
- (2) Thereafter, while the pressure drops, the total contact *force* continues to rise. During this time, damage bands in an approximately conical configuration emanate from the intense damage zone directly beneath the impact. In addition, damage, representative of radial cracking, initiates at the

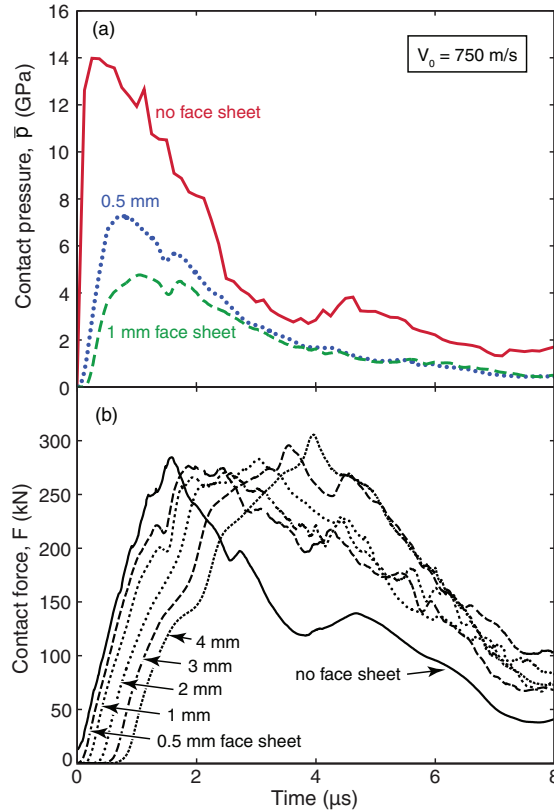


Figure 12. Effects of face sheets on histories of (a) average contact pressure and (b) contact force.

tile backface and grows upwards through the tile. Then, once the projectile begins to rebound, the contact force diminishes and the damage evolution process once again seemingly ceases.

- (3) In the final stage, the ceramic tile itself undergoes a form of rebound, placing the impacted surface (and most importantly the damaged zone) into a state of biaxial tension. Damage growth then resumes at this location. In the present example, this event occurs about $17 \mu\text{s}$ after impact. It should be noted that the prediction of damage in this stage may be an artifact of the axisymmetric nature of the model. That is, in reality, the hoop stresses could be relieved by radial cracking rather than further diffuse damage growth. Indeed, such cracking is observed in the tiles tested in the high velocity domain. This feature, however, cannot be captured by the present (axisymmetric) model.

The role of a metal face sheet is illustrated in [Figure 12](#). Its main effect is to increase the effective contact area on the top surface of the ceramic (at the interface with the face sheet) and hence lower the contact pressure ([Figure 12a](#)). Plots of the local contact pressure distribution on the ceramic surface at various times during the impact confirm this ([Figure 13](#)). In turn, the predicted size of the damage zone diminishes. The experimental results provide confirmation of this effect. The reduced pressure also leads to reduced plasticity and hence a shallower impact crater, as shown in [Figure 5](#).

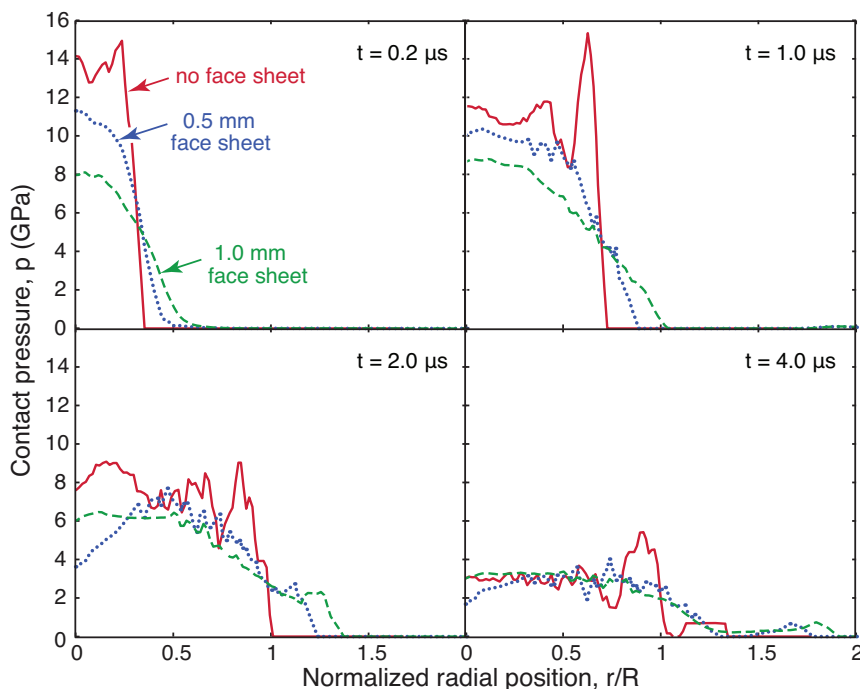


Figure 13. Contact pressure distributions at various times after impact. Impact velocity is 750 m/s. Time is measured from the instant that stresses reach the ceramic surface.

The finite element results further show that the face sheet does *not* significantly affect the maximum force imparted to the ceramic (Figure 12b). This result, along with the experimental observation that face sheets do not affect the degree of back-face radial cracking (Figure 3), strongly suggests that such cracking is dictated predominantly by the maximum contact force, as opposed to the contact pressure. This is supported by the results of a recent numerical study [Compton et al. 2011], demonstrating that the maximum back-face hoop stress in a supported tile under impact loading is essentially the same as that obtained under quasi-static loading at the same contact force.

5. Summary and conclusions

The material parameters in the extended Deshpande–Evans constitutive model have been calibrated for an armor alumina through a combination of independent property measurements, judicious selection of parameter ranges when direct measurement is not feasible, and comparisons of parametric numerical studies with experimental measurements and observations. The model has been shown to predict reasonably accurately the variation in the size of the comminuted zone beneath the impact site with impact velocity as well as secondary damage processes such as those manifested as cone and radial cracks. The evolution of damage and cracking has been explained in terms of the contact pressure and force evolution throughout the impact: the microcrack damage zone develops with the contact pressure, while the secondary cracking develops with the contact force and structural rebound of the tile. The numerical simulations have also provided new insights into the role of metal face sheets on the damage processes.

Specifically, these sheets aid in distributing the load over a larger area in the early stages of impact, when the peak contact pressures are attained, and thus reduce the propensity for microcracking as well as lattice plasticity. But, for the thicknesses employed here, they do not significantly affect the peak contact force transmitted to the underlying ceramic tile and thus have no apparent effect on the degree of radial and cone cracking. The expectation is that, for larger values of normalized sheet thickness, h/R , the latter processes may be affected.

In its present implementation, the model is restricted to 2D loadings and is thus unable to capture features that break radial symmetry. Most notably, it cannot predict the radial cracks that occur on both the impacted face and the back face. This deficiency has been mitigated recently through the implementation of a 3D version of the constitutive model by Radovitzky and co-workers for use in 3D simulations (R. Radovitzky, private communication). The latter simulations do indeed predict the formation of radial cracks during an impact event. The results of that study will be reported elsewhere.

Acknowledgements

Support from the Office of Naval Research through a Multidisciplinary University Research Initiative Program on “Cellular Materials Concepts for Force Protection,” Prime Award No. N00014-07-1-0764, is gratefully acknowledged. EAG was supported by a National Defense Science and Engineering Graduate Fellowship.

References

- [Aeberli and Rawlings 1983] K. E. Aeberli and R. D. Rawlings, “Effect of simulated body environments on crack propagation in alumina”, *J. Mater. Sci. Lett.* **2**:5 (1983), 215–220.
- [Ashby and Hallam 1986] M. F. Ashby and S. D. Hallam, “The failure of brittle solids containing small cracks under compressive stress states”, *Acta Metall.* **34**:3 (1986), 497–510.
- [Ashby and Sammis 1990] M. F. Ashby and C. G. Sammis, “The damage mechanics of brittle solids in compression”, *Pure Appl. Geophys.* **133**:3 (1990), 489–521.
- [Chantikul et al. 1990] P. Chantikul, S. J. Bennison, and B. R. Lawn, “Role of grain size in the strength and R-curve properties of alumina”, *J. Am. Ceram. Soc.* **73**:8 (1990), 2419–2427.
- [Compton et al. 2011] B. G. Compton, E. A. Gamble, and F. W. Zok, “Failure initiation during impact of metal spheres onto ceramic targets”, 2011. Submitted to *Int. J. Impact Eng.*
- [Denzel 2010] J. R. Denzel, “Determination of shock properties of ceramic corbit 98: 98% alumina”, Master’s thesis, Naval Postgraduate School, Monterey, CA, June 2010, Available at <http://hdl.handle.net/10945/5312>.
- [Deshpande et al. 2011] V. S. Deshpande, E. A. N. Gamble, B. G. Compton, R. M. McMeeking, A. G. Evans, and F. W. Zok, “A constitutive description of the inelastic response of ceramics”, *J. Am. Ceram. Soc.* **94**:S1 (2011), 204–214.
- [Gamble et al. 2011] E. A. Gamble, B. G. Compton, V. S. Deshpande, A. G. Evans, and F. W. Zok, “Damage development in an armor ceramic under quasi-static indentation”, *J. Am. Ceram. Soc.* **94**:S1 (2011), 215–225.
- [Horii and Nemat-Nasser 1986] H. Horii and S. Nemat-Nasser, “Brittle failure in compression: splitting, faulting and brittle-ductile transition”, *Phil. Trans. R. Soc. A* **319**:1549 (1986), 337–374.
- [Longy and Cagnoux 1989] F. Longy and J. Cagnoux, “Plasticity and microcracking in shock-loaded alumina”, *J. Am. Ceram. Soc.* **72**:6 (1989), 971–979.
- [Rhee et al. 2001] Y.-W. Rhee, H.-W. Kim, Y. Deng, and B. R. Lawn, “Brittle fracture versus quasi plasticity in ceramics: a simple predictive index”, *J. Am. Ceram. Soc.* **84**:3 (2001), 561–565.
- [Shih et al. 2000] C. Shih, M. A. Meyers, V. F. Nesterenko, and S. J. Chen, “Damage evolution in dynamic deformation of silicon carbide”, *Acta Mater.* **48**:9 (2000), 2399–2420.

[Stout and Follansbee 1986] M. G. Stout and P. S. Follansbee, “Strain rate sensitivity, strain hardening, and yield behavior of 304L stainless steel”, *J. Eng. Mater. Technol. (ASME)* **108**:4 (1986), 344–353.

Received 27 Feb 2012. Accepted 16 Mar 2012.

BRETT G. COMPTON: bcompton@engineering.ucsb.edu

Materials Department, University of California, Santa Barbara CA 93106-5050, United States

ELEANOR A. GAMBLE: nell.gamble@gmail.com

Materials Department, University of California, Santa Barbara CA 93106-5050, United States

VIKRAM S. DESHPANDE: vsd@eng.cam.ac.uk

Engineering Department, Cambridge University, Trumpington Street, Cambridge, CB2 1PZ, United Kingdom

FRANK W. ZOK: zok@engineering.ucsb.edu

Materials Department, University of California, Santa Barbara, Santa Barbara CA 93106-5050, United States

<http://engineering.ucsb.edu/~zok/zok.html>

JOURNAL OF MECHANICS OF MATERIALS AND STRUCTURES

jomms.net

Founded by Charles R. Steele and Marie-Louise Steele

EDITORS

CHARLES R. STEELE Stanford University, USA
DAVIDE BIGONI University of Trento, Italy
IWONA JASIUK University of Illinois at Urbana-Champaign, USA
YASUHIRO SHINDO Tohoku University, Japan

EDITORIAL BOARD

H. D. BUI École Polytechnique, France
J. P. CARTER University of Sydney, Australia
R. M. CHRISTENSEN Stanford University, USA
G. M. L. GLADWELL University of Waterloo, Canada
D. H. HODGES Georgia Institute of Technology, USA
J. HUTCHINSON Harvard University, USA
C. HWU National Cheng Kung University, Taiwan
B. L. KARIHALOO University of Wales, UK
Y. Y. KIM Seoul National University, Republic of Korea
Z. MROZ Academy of Science, Poland
D. PAMPLONA Universidade Católica do Rio de Janeiro, Brazil
M. B. RUBIN Technion, Haifa, Israel
A. N. SHUPIKOV Ukrainian Academy of Sciences, Ukraine
T. TARNAI University Budapest, Hungary
F. Y. M. WAN University of California, Irvine, USA
P. WRIGGERS Universität Hannover, Germany
W. YANG Tsinghua University, China
F. ZIEGLER Technische Universität Wien, Austria

PRODUCTION contact@msp.org

SILVIO LEVY Scientific Editor

Cover design: Alex Scorpan

Cover photo: Ev Shafir

See <http://jomms.net> for submission guidelines.

JoMMS (ISSN 1559-3959) is published in 10 issues a year. The subscription price for 2012 is US\$555/year for the electronic version, and \$735/year (+ \$60 shipping outside the US) for print and electronic. Subscriptions, requests for back issues, and changes of address should be sent to Mathematical Sciences Publishers, Department of Mathematics, University of California, Berkeley, CA 94720–3840.

JoMMS peer-review and production is managed by EditFLOW[®] from Mathematical Sciences Publishers.

PUBLISHED BY
 **mathematical sciences publishers**
<http://msp.org/>

A NON-PROFIT CORPORATION

Typeset in L^AT_EX

Copyright ©2012 by Mathematical Sciences Publishers

- The implicit corotational method and its use in the derivation of nonlinear structural models for beams and plates**
GIOVANNI GARCEA, ANTONIO MADEO and RAFFAELE CASCIARO 509
- Nonlinear FEM analysis for beams and plate assemblages based on the implicit corotational method**
GIOVANNI GARCEA, ANTONIO MADEO and RAFFAELE CASCIARO 539
- Damage development in an armor alumina impacted with ductile metal spheres**
BRETT G. COMPTON, ELEANOR A. GAMBLE, VIKRAM S. DESHPANDE and FRANK W. ZOK 575
- An asymptotic method for the prediction of the anisotropic effective elastic properties of the cortical vein: superior sagittal sinus junction embedded within a homogenized cell element**
RANIA ABDEL RAHMAN, DANIEL GEORGE, DANIEL BAUMGARTNER, MATHIEU NIERENBERGER, YVES RÉMOND and SAÏD AHZI 593